Applied Ocean Research 129 (2022) 103370

Contents lists available at ScienceDirect

Applied Ocean Research

journal homepage: www.elsevier.com/locate/apor

The influence of infragravity waves, wind, and basin resonance on vessel movements and related downtime at the Outer Port of Punta Langosteira, Spain

Raquel Costas [a,*], Andrés Figuero [a], José Sande [a], Enrique Peña [a], Andrés Guerra [b]

[a] Water and Environmental Engineering Group (GEAMA), University of A Coruña, Campus Elviña s/n, A Coruña 15071, Spain
[b] Port Authority of A Coruña, Avenida de La Marina 3, A Coruña 15001, Spain

ARTICLE INFO

Keywords:
Infragravity waves
Moored vessel motions
Wavelet transform analysis
Vessel resonance
Operational thresholds
Downtimes

ABSTRACT

The coupling of low-frequency oscillatory modes of a harbor with horizontal motions of moored ships can amplify the latter, causing operational and safety problems. The objectives of this study were to analyze infragravity waves and their effect on moored ship motions; to validate the Wavelet Transform Analysis (WTA) method for studying port-ship resonance in the Outer Port of Punta Langosteira, Spain; and to study the climatic forcing of downtimes. The excited resonant modes of the basin (102 and 132 s) were determined using a numerical model and high-frequency water level measurements at different points of the harbor. Yaw and sway motions of three bulk carriers were analyzed in the frequency-time domain using WTA. The results showed that the oscillation periods of the studied vessel motions are directly related to the water depth to vessel draft ratio. In addition, when the wind speeds exceeds 20 km/h, the ship moves away from the fenders, which lead to a lengthening of these periods. Based on our findings, yaw may induce oscillations of the same period in sway. Additionally, operational thresholds were proposed based on outer and inner waves data that will lead to optimize ship stays, avoiding downtimes, and to advance the safety of loading and unloading operations.

1. Introduction

Infragravity waves (IG) are waves with frequencies lower than those generated by the wind (short wave), with periods between 30 s and 5 min (Herbers et al., 1995). These oscillations are generated by different mechanisms. The most common factors are those related to atmospheric disturbances as wind (Niu, 2020; Ayet and Chapron, 2022) and non-linear short wave interactions (Thiebaut et al., 2013; Gao et al., 2017, 2021; Bertin et al., 2018; Seetharam et al., 2022). In the ocean, waves usually have a wide spectrum of frequencies. If waves enter a semiclosed physical domain, such as a port, the energy of a set of frequencies is amplified. These frequencies coincide with the natural oscillation periods of the port and are known as resonant or eigenmodes (Rabinovich, 2009). Thus, IG waves at a berth depend on the wave height outside the port and on the amplification inside the port (Weiler and Dekker, 2001). The presence of IG waves in a port can be amplified due to resonance and therefore can be dangerous to moored ships (Thotagamuwage and Pattiaratchi, 2014). Motions can increase when the natural period of oscillation of the ship is close to the period of the waves (van der Molen et al., 2006). Therefore, long waves can excite horizontal motions (yaw, sway and surge) because their oscillation period is in the IG band (López et al., 2012). These motions are the most relevant for security and operability (van der Molen et al., 2015). Consequently, reducing the dynamic response of ships increases productivity and, thus, profits (van Deyzen et al., 2015).

Long wave and port resonance have long been studied (Wilson, 1954; Chen et al., 2006; Wang et al., 2011). Some authors aimed at determining their generation and amplification processes (Mei and Agnon, 1989; Sammartino et al., 2014; Karathanasi et al., 2020; Bellotti, 2020), whereas others conducted research on how to reduce the amplitudes of infragravity waves in ports: Geraldton, Australia, (van Dongeren et al., 2016), Mukho, Korea, (Kwak et al., 2020) or in NGqura, South Africa (Troch et al., 2020b). Many studies focused on long wave prediction (Diaz-Hernandez et al., 2015; André et al., 2021). Moored ship motions and their relationship with infragravity waves have been analyzed from different perspectives. Based on numerical results (Sakakibara and Kubo, 2008) and physical tests (Nogueira et al., 2018), these studies confirmed that, when the response peak of a motion coincides with the

* Corresponding author.
E-mail address: raquel.costas.gomez@udc.es (R. Costas).

https://doi.org/10.1016/j.apor.2022.103370
Received 22 March 2022; Received in revised form 5 October 2022; Accepted 5 October 2022
Available online 13 October 2022

oscillation period of the port, the motion amplitude is greatly magnified. In addition, the location of the ship in the harbor must be considered because it affects the waves system and therefore the motion responses (van der Molen et al., 2004; Rupali et al., 2021). Longitudinal forces are stronger near nodes and weaker near antinodes (Weiler and Dekker, 2001). Therefore, the motions are greater when the berth location is close to a node, as shown by Troch et al. (2020a) with real data and a numerical model in the port of Cape Town, South Africa. You and Faltinsen (2015) demonstrated that the linear horizontal motions of a moored ship are greater in shallower water depths. Subsequently, a numerical model showed that motion amplitude decreased with the increase in factor δ (water depth/vessel draft) due to changes in the resonant periods, for example, in Paradip Port, India (Gulshan et al., 2020). Similarly, the mooring system is crucial because it can be applied to control ship motions (Nogueira et al., 2018). Many studies suggest that mooring lines break mainly because of motions caused by infragravity waves (López and Iglesias, 2014; van Deyzen et al., 2015). However, some aspects and variables remain overlooked, such as the wind effect on the position of the ship and consequently on the movements, raised in this study, or the process whereby one vessel motion induces another in port-ship resonance. The study by van der Molen et al. (2015) suggested that a secondary peak in sway motion results from a coupling between sway and yaw.

Studies published in the literature extensively cover research on moored ship motions in the frequency domain. However, analysis in the time-frequency domain is essential to fully account for the nonlinear effects and time-frequency variation of exciting forces, as well as the motion response of the moored vessel (Yu et al., 2006; Gaythwaite, 2014). Despite it being well-known that time-frequency should be analyzed, and the available techniques, such as wavelet transform (Loughlin and Cohen, 2010), this type of analysis in moored ship motion studies is rare.

Costas et al. (2022) exemplify this application to the surge motion of liquefied petroleum gas (LPG) carriers during their operation in the Inner Port of A Coruña, Spain. As stated therein, the range of climatic conditions was relatively narrow, as well as the fleet and mooring configurations, reducing the number of study variables.

Port-ship resonance is also a problem highly dependent on the characteristics of each port and on the location of each berth (Gulshan et al., 2020; Troch et al., 2020a). The increasing size of ships forces the construction of new and deeper ports, but deep areas do not dissipate as much energy as shallow water, thereby increasing the hydrodynamic complexity (Feng et al., 2020). Moreover, a multipurpose terminal with a continuous berth offers multiple berth location and mooring configuration options for vessels of different sizes. Combined with the increased hydrodynamic complexity and the possibilities of the multipurpose terminal significantly increase the complexity of the problem and the number of influencing variables. For all these reasons, comprehensive research studies on port-ship resonance in the time-frequency domain should be conducted, as much as possible, in field campaigns with measured data.

Considering the above, this study presents a comprehensive analysis of port-ship resonance in a large basin, the Outer Port of Punta Langosteira (A Coruña, Spain). The main objective is to learn more about this problem, to optimize ship stays, avoiding downtimes, and to advance the safety of loading and unloading operations. For this purpose, harbor resonant modes were assessed using a numerical model, validating excited frequencies with wave measurements in the field to determine the spatial distribution of nodes and antinodes. The recorded sway and yaw motions of three bulk carriers moored at two areas of the studied berth were analyzed along with the concomitant weather in the time-frequency domain by Wavelet Transform Analysis (WTA). The effects of infragravity waves, tide, progress in loading condition of the vessel and wind on variations in the oscillation period and energy of the motions was determined. Applying WTA made it possible to study port-ship resonance in time and to assess the time evolution of amplitudes of the moored vessel motions that cause mooring lines breakage. Furthermore, the meteorological forcing causing twelve downtime intervals occurred in the studied port between 2017 and 2020 were studied and operational thresholds were proposed.

The general structure of this work consists of four sections organized as follows: Section 2 presents the study area and the available field data, as well as the data analysis methods used in this study; Section 3 shows and discusses the findings, from both hydrodynamic and from moored ship motion perspectives. Last, Section 4 presents the conclusions and final observations.

2. Materials and methods

2.1. Study area

The Outer Port of Punta Langosteira is located on the northwestern tip of the Iberian Peninsula, specifically in the municipality of Arteixo (A Coruña, Spain) (43° 21′ 27.6" N; 8° 23′ 13.7" W) (Fig. 1a and b). Because this port is located on the Atlantic coast, the waves are some of the most energetic in Europe, given the presence of low pressure systems in the Atlantic Ocean (Lorente et al., 2018). According to the wave buoy *Boya Langosteria II* (Puertos del Estado (Spanish Port Autority), 2022) (43° 21′ 0" N 8° 33′ 36" W) (Fig. 1b), the dominant swell direction is NW, which occurs 46.12% of the time, followed by NNW (26.87%), N (12.86%) and WNW (11.07%) directions. The average significant wave height of the storms (99.86% probability of non-exceedance or return period of one year) is 6.2 m. Similarly, the wind mainly blows from the NNE-NE and SW-SSW directions, with storm speeds averaging 71.25 km/h (99.86% probability of non-exceedance).

To shelter from these climatic conditions, this port consists of the main breakwater and the secondary breakwater. The 3360 m-long main breakwater, arranged in three alignments, is protected by a 150-T concrete cube main armor and rises from a maximum depth of -43–+25 m of its berm crest. The 1320 m-long secondary breakwater contains a 45-T Cubipod armor. The harbor formed by both breakwaters has an almost rectangular shape with 270 hectares of sheltered water. The dock areas of berth A1 and berth A3 (Fig. 1c), arranged in an 118° direction, are operational. Additionally, berth B is located in the 208° direction. The 900 m-long berth A1 has a mean water depth of 22 m, whereas the 300 m-long berth A3 has a mean water depth of 15.5 m. Given its length (1200 m), the area of operations was divided into different berth areas to facilitate the analysis (berth A1: Z4, Z5, Z6; berth A3: Z3) (Fig. 1c). General cargo ships and bulk carriers ranging from 2600 to 93000 DWT (Deadweight tonnage, vessel's weight carrying capacity), with length overalls between 80 and 220 m, are usually moored at these berths. Larger ships are mainly moored at berth A1 because its water depth is deeper (30 m).

2.2. Field campaign

Considering the characteristics of the port and the different sizes of the fleet (higher number of influencing variables than in a specialized terminal), *in situ* data collection becomes essential in this study. For this reason, a field campaign was conducted to collect marine weather data (waves and wind) and moored ship motion data in berth A1. During loading and unloading operations, sway and yaw motions were recorded. The mooring configuration of the monitored vessels was also available. Additionally, information of 12 intervals of port downtime was obtained, of which 6 resulted in departure from the berth to anchor.

Wave data were collected both outside the port and inside the harbor. The outer buoy is included in the Coastal Buoy Network of Puertos del Estado (*Red de Boyas Costera de Puertos del Estado* – REDCOS) (43° 21′ 0" N 8° 33′ 36" W) (Fig. 1b) and provides the parameters that define hourly sea states (significant wave height, peak period and direction). The tide gauge Miros radar (2022) is installed at the spur breakwater of the main breakwater and records data at a 2 Hz frequency, whereas the

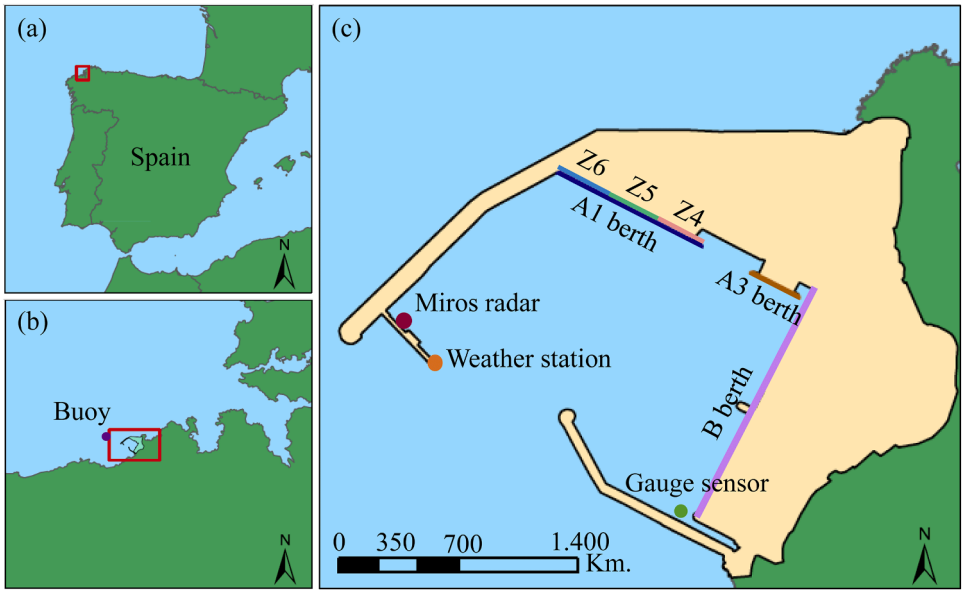

Fig. 1. (a) Spain showing the location of A Coruña, (b) location of the port, (c) plan view of the Outer Port of Punta Langosteira and location of the measurement equipment.

pressure gauge at the inner side of the secondary breakwater records at 1 Hz (Fig. 1c). Ten-minute wind speed and direction data were gathered from the meteorological station located on the spur breakwater of the main breakwater (Fig. 1c). Wave data outside the port and wind data are available from Puertos del Estado Autoridad Portuaria de A Coruña (2021).

Moored ship motions were assessed by installing two laser distance measurers, one at the bow and one at the stern of each ship, following the method used by our research group in previous studies (Peña et al., 2017; Sande et al., 2019; Figuero et al., 2019). Thus, in addition to bow, stern and midship sway, yaw was determined in all ships under study. The characteristics of these three bulk carriers, as well as berth and operational data, are outlined in Table 1. Additionally, the average and maximum marine weather conditions recorded during the monitoring period are presented in Table 2.

2.3. Application of the numerical model

The oscillation periods or resonant modes of the port under study were determined using a numerical model, which solves the stationary patterns of wave propagation based on the elliptic mild-slope equation. These models reproduce the standing wave patterns within numerical domains of complex geometries based on boundary condition forcings. Therefore, for an incident wave within a range of frequencies, the model provides the amplification of the oscillations.

The model applied in this study was the Mild Slope Ports-IHCantabria (MSPv1.0) used in previous studies (Diaz-Hernandez et al., 2015, 2021). This is a wave propagation model that solves the two-dimensional horizontal (2DH) stationary patterns of free surface and wave height of different forcings within numerical domains (bathymetry and real contours), defined by adaptive meshing for finite element analysis (finite element method – FEM). Bathymetry was obtained by integrating detailed bathymetric data within the port and at the entrance, provided by the Port Authority of A Coruña (Autoridad Portuaria de A Coruña) and the general bathymetry downloaded from European Marine Observation (EMODnet, 2022). The latter was added to expand the domain, primarily to include the shoals located WSW and NW of the head of the main breakwater (Fig. 2) for their possible effect on wave propagation.

The contours were defined at the still water line, in the port area, and in the wave generation area, located up to 0.5 L out to sea from the first obstacle (main breakwater), being L the longest propagation wavelength. Because this was a resonance study, the reflection coefficient of the port contours was set at 1 and that of the water contours leading to the generation zone at 0 (Fig. 2a). With this information, the model created the propagation mesh with the target period of 35 s (one of the shortest propagated) by subdividing the domain into smaller sections (finite elements), thus, generating a discretized space to perform the calculations.

The forcings introduced were 150 monochromatic wave cases, resulting from the combination of a wave height of 0.25 m (usual long wave value) with a sweep of periods between 30 and 180 s. To assess direction and tide level effects, these cases were propagated in the main wave direction (NW) (Section 2.1) and in the directions closest to NW (NNW and WNW) at three tide levels: mean higher high water (MHHW), mean lower low water (MLLW), and mean sea level (MSL). Wave-breaking, white-capping, and nonlinear quadruplet wave-wave interactions were disabled when running the model, given that such effects will not have a critical influence in the modelled situation.

The outputs of this model were resonance maps and curves, that is, the value of the amplification factor at each period in each place. These results were normalized based on the simulated incoming wave height (0.25 m). The aim of the model application to obtain the resonance maps was achieved, so the curves were used for the validation of peak

Table 1
Vessels and monitoring campaign details. Mooring lines in the following order: Lines (fore-aft), spring lines (fore-aft), and breast (fore-aft).

Vessel characteristics				Monitoring data			
Name	DWT (t)	Overall length (m)	Beam (m)	Operation	Zone	Total time (h)	Mooring lines
Nord Saturn	77288	225	32.26	Unloading	5	60	4-6-2-2-0-0
Nautical Lucia	63548	200	32.25	Loading	5	50	4-4-2-2-0-0
Aloe	30618	179	28	Unloading	4	51	4-4-3-3-2-2

Table 2
Average and maximum sea-state and marine weather data outside and inside the port during vessel monitoring time.

Vessel	Buoy					Miros radar			Weather station	
	H_s max (m)	H_s mean (m)	T_p max (s)	T_p mean (s)	Average direction (°)	H_s max (m)	H_s mean (m)	Tidal range (m)	Mean wind speed (km/h)	Mean wind direction (°)
Nord Saturn	6.66	3.66	15.40	12.73	290	0.49	0.28	0.66-3.37	25	77
Nautical Lucia	2.03	1.56	12.68	10.76	309	0.25	0.17	0.79-3.44	10	150
Aloe	3.73	2.89	18.20	14.75	308	0.34	0.27	0.67-3.68	27	39

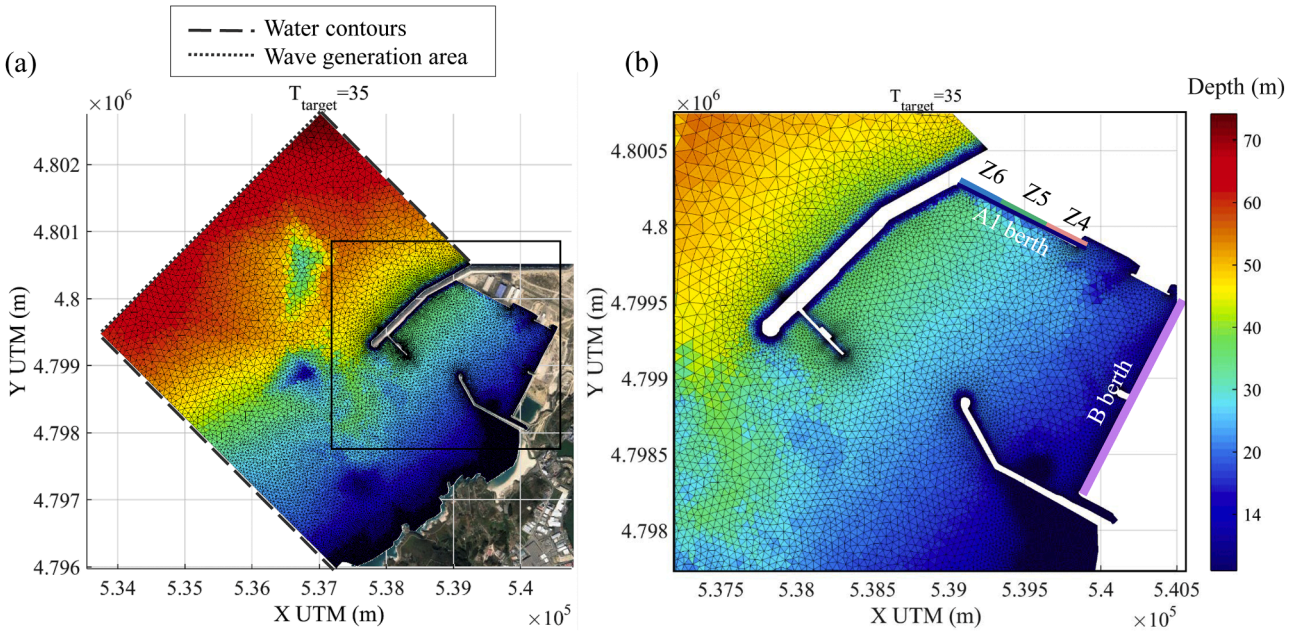

Fig. 2. (a) propagation FEM mesh generated with 35 s target period by MSP model and (b) zoom of the mesh in the harbor area.

frequencies. Validation was performed with data from the Miros radar and pressure gauge located at the inner side of the secondary breakwater. The distributions of nodes and antinodes made it possible to determine the response of the port to the incident energy in the infragravity band, thereby assessing their effect on moored ship motions.

2.4. Data analysis

The data recorded in the field campaign, both sea-level oscillations and moored ship motions, were analyzed in the frequency and time-frequency domains by fast Fourier transform (FFT) and by wavelet transform analysis (WTA), respectively. The joint implementation has already been used in concomitant wave and surge motion records, providing enlightening results, in a nearby port by the authors of this study (Costas et al., 2022). It allowed to investigate the influence of the δ (water depth/vessel draft) and to detect that the surge motion of identical vessels usually entered into resonance just in one of two adjacent jetties, causing this berth more dangerous.

FFT is widely known in data processing, including in moored ship analysis (Pessoa et al., 2015; Nielsen, 2017). This tool presents the energy of a signal in the frequency domain, assuming a stationary signal and therefore does not provide information over time (Massel, 2001). In turn, non-stationary signals whose energy changes in magnitude and/or frequencies over time, such as those of waves or ship motions, require studying in the time-frequency domain. Some authors apply different methods for wave analysis such as spectrograms (Hwang et al., 2003; López et al., 2012; Stuart et al., 2014) or Hilbert-Huang transform (Kumar and Mandal, 2022; Hao and Shen, 2022). However, wavelet transform analysis has been proposed as the superior analysis method since uses shifted window depending on frequency as expose (Loughlin and Cohen, 2010).

The wavelet transform spectrum is generated by signal convolution and a scaled and shifted mother function. This mother function is scaled to adapt to the different analysis frequencies and is shifted the entire recording period. The Morlet function is the most appropriate mother function for this purpose given the characteristics of the wave records (Liu, 1994) and, by analogy, is also considered appropriate for ship motions. The result may be visualized as a color graph, which represents the energy on the axis of periods (ordinates) and on the axis of time (abscissa). In this case, periods between 4 and 300 s were analyzed and the time axis was preserved with the sampling intervals of the input signal. In this representation, the logarithm of energy (normalized to the maximum value of each wavelet plot) is shown in the color scale from blue to red, with the maximum values in red and the minimum in blue. Therefore, WTA represents energy packets in the time-frequency domain. The FFT spectrum is equivalent to the average wavelet spectrum over the same observation period (Díaz-Hernández, 2006).

The WTA method enables the energy localization in the time-frequency domain and, therefore, presents a significant advance in new perspectives for signal analysis. In this study, the method described in Torrence and Compo (1998) with modifications by Liu et al. (2007) was applied, whereby wavelet coefficients are converted into energy for comparison between frequencies.

Complementarily, the amplitudes of each individual wave included in the recorded time series were obtained with the distance between the minimum and maximum values with an intermediate zero crossing. With this, the significant amplitude of the movement was determined, that is, the mean of the major third of each hour. Moreover, the wave

record was decomposed into three signals using a window filter. This window filter allows to set the periods range for extracting the signal. Long waves were divided into infragravity waves (IG) and far infragravity waves (FIG). The following limits were used to define the ranges: swell (4–30 s), IG (30–150 s) and FIG (150–300 s).

3. Results and discussion

To assess the effect of infragravity waves (30–150 s) on the behavior of moored ships, the analysis of the harbor hydrodynamics is presented in this section, particularly focusing on the IG band and on its relationship with two motions, namely, sway and yaw. The numerical model MSP described above was applied to analyze the long wave, in combination with data from the tide gauge and the pressure gauge installed inside the harbor (Fig. 1c). This model provided the resonant maps and the amplification factor at the desired points. Based on these results, the dynamic response of the sway and yaw motions of the three ships monitored in berth A1 was analyzed and discussed. Their behavior in the time-frequency domain was investigated by WTA. The effect of the wind action was assessed by analyzing the evolution of its intensity and direction over time as a particularly novel feature of this study. In addition, the climatic variables of waves, wind and tide during twelve downtimes were analyzed. This will be worked out in the following three sections.

3.1. Hydrodynamics

The wave amplification factor was calculated at different locations: at the central points of zones Z4, Z5 and Z6 of berth A1 and at the locations of the Miros radar and pressure gauge (Fig. 1c). On the one hand, the resonance curves of the location of the equipment were used to validate the model and, on the other hand, those obtained in the berth were used to analyze the motions of the ships.

The energy spectra calculated from Miros radar and pressure gauge data recorded over a 24 h period were represented together with the modeled amplification factor for a situation including the mean sea level at the same location (Fig. 3a and b). The magnitude comparison is qualitative because the value of the amplification factor is represented in terms of relative wave height, whereas the spectra of the records are displayed in terms of spectral density and but also because the peak magnitudes have no physical meaning due to the absence of dumpling in the numerical model. However, the correct functioning of the model for calculating resonant periods was verified since they coincide with the periods calculated by FFT of the records, therewith confirming the correct modelling of water depths and horizontal geometry dimensions.

The energy spectra show 100 and 132 s as the most energetic periods within the IG band in both instruments. Similarly, these peaks are presented in the results of the model. The latter also shows amplification peaks at higher frequencies: at 40 s at both locations, at 34 and 64 s at the pressure sensor, and finally at 76 s at the tide gauge. However, the spectra obtained from field records show significantly lower energy at these periods than in 102 and 132 s, most likely because the infragravity energy that reaches the port is mostly concentrated in the low-frequency region of the spectrum. As such, these more energetic periods are excited inside the port, amplifying the associated wave. Long wave energy inside a harbor may be amplified if the period of the incoming waves is close to the resonant period of the harbor (van der Molen et al., 2004; Thotagamuwage and Pattiaratchi, 2014). This hypothesis could be verified in future studies with spectral data collected outside the port.

The resonant periods described in this study vary with the tide level: the higher the water depth is, the shorter the periods will be, and vice versa. Considering the tidal range in the study location, 4.35 m (see Section 2.1), the period of 102 s varies between 97 and 108 s and the period of 132 s between 124 and 136 s, in mean higher high water (MHHW) and mean lower low water (MLLW), respectively. The same correlation applies to shorter periods, albeit with a smaller range of variation. For example, the peak period of 40 s varies between 37 and 41 s. The direction of the incident waves does not influence these periods, and only slightly modifying its magnitude, which is to be expected for such long waves as considered here.

To understand the behavior of infragravity waves in berth A1, the amplification factors at the central points of the three zones into which this berth is divided (Fig. 1c) were determined and represented. These results of the mean sea level indicate peaks at 102 and 132 s, as shown in Fig. 4, highlighted in the results for the location of the tide gauge, are also important in the berth A1; the peak at 102 s is more relevant in zone 6; and the peak at 132 s, in zones Z4 and Z5. Additionally, albeit less relevant because of the lack of response found in practice in the port due to the absence of long wave energy supply at those frequencies, the following peaks at the corresponding periods stand out in the respective zones: 34 s in Z4, 40 s in Z4 and Z5, and 76 s in Z5. Since an amplification factor strongly depends on the location, maps of these resonant modes are analyzed in order to understand their spatial arrangement and their effect on moored ship motions.

The resonance maps (Fig. 5) show the distribution of the nodes (minimum vertical amplification) and antinodes (maximum vertical amplification) in the harbor, that is, they represent the amplification factor in the space domain. Considering the results from the resonance curves, the previously highlighted periods of the different areas of berth A1 have been selected for analysis (Fig. 4): 34, 40, 76, 102 and 132 s.

The shorter periods (34 and 40 s) generate greater amplifications in berth B (secondary breakwater-berth A3) than in other areas of the harbor, a behavior that is not seen in the maps of longer periods. Both resonant modes form three antinodes and two intermediate nodes along

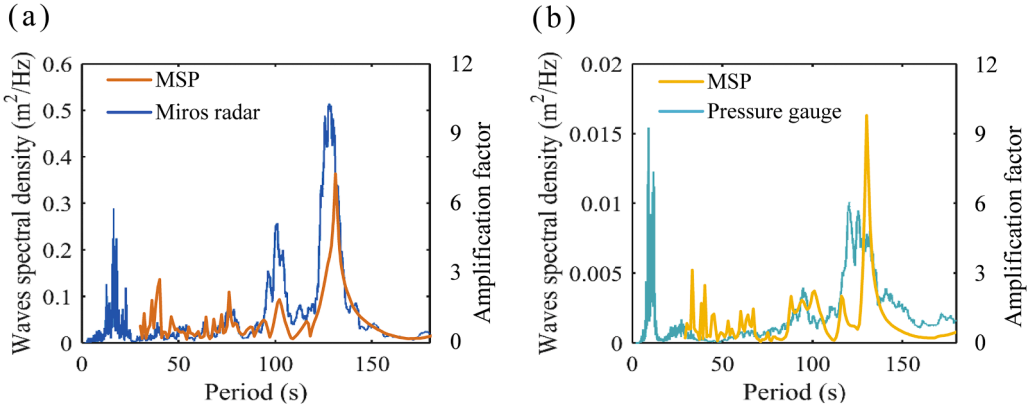

Fig. 3. Validation of the MSP amplification factor obtained for mean sea level with the spectrum from (a) the Miros radar record of 11/17/2018 and from (b) the gauge sensor record of 06/01/2018.

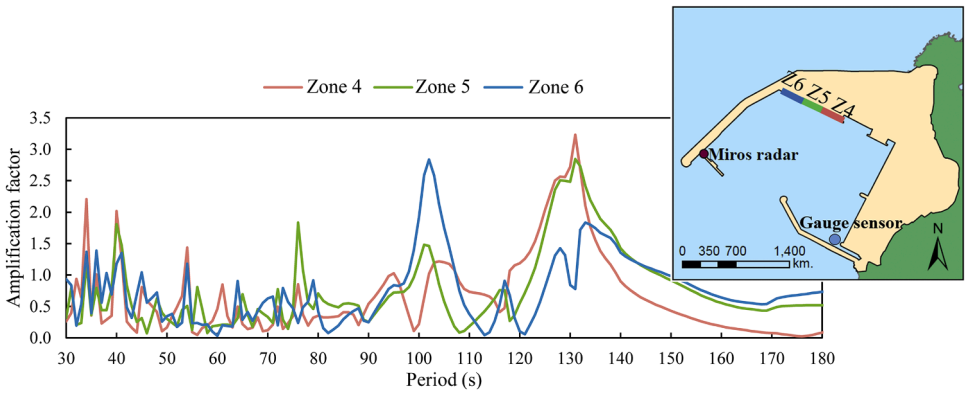

Fig. 4. Resonance curves as a function of period at the zones Z4, Z5 and Z6 of berth A1.

berth A1 (Fig. 5a and b) since their wavelengths at 22 m of depth are 487 and 577 m (for 34 s and 40 s, respectively), and the berth measures 900 m. The 76 s resonant mode presents an antinode between zones Z4 and Z5 and a node in zone Z6; in this case, the wavelength (1110 m) is slightly longer than the berth length.

For the 102 s resonant mode, since the wavelength (1494 m) is approximately 1.5 times the length of the berth, the antinode is located at the corner of berth A1 with the main breakwater (Z6), generating the node in Z4 and the transition in Z5. Last, the 132 s resonant mode flow moves in the main breakwater-berth B direction (area aligned with the coast). Thus, this resonant mode flow forms an antinode at the corner of the tide gauge that reaches the entire third alignment of the main breakwater, another antinode along berth B and a central antinode between them. Since the wavelength (1935 m) is approximately 2 times the length of this berth, the entire berth line is affected by this antinode, with the maximum amplification in Z4 and the minimum in Z6.

In the antinode zones, the wave vertical velocity peaks, which increases the amplitudes of vertical motions of the moored ships. In contrast, the wave horizontal velocity peaks in the nodes, increasing the amplitudes of horizontal motions. The low resonant modes (34, 40 and 76 s) could be more relevant for port-ship resonance effects because they are in the same frequency range of the horizontal oscillations of ships (López et al., 2012). However, these resonant modes do not show a marked energy in the spectra of the instrumental records, unlike the periods of 102 and 132 s (Fig. 3). As stated above, they show low energy because the energy that comes from the outside is likely bound at lower frequencies and, consequently, excites the resonant modes with longer periods, which should also occur in the berth, with the highest energy modes at 102 and 132 s.

Therefore, due to the distribution of nodes and antinodes, the maximum horizontal velocity is found at Z6 for the 132 s resonant mode and at Z4 for the 102 s mode. In addition, zone Z5 shows an intermediate behavior, being affected in both axes (horizontal and vertical) for both cases (102 and 132 s modes).

Last, the model accurately determines the resonant periods, so its results are appropriate for the analysis proposed in this study. Based on this information and on Miros radar and pressure gauge spectra, at berth A1, the resonant modes with periods of 34, 40 and 76 s are not excited. Similarly, the 102 and 132 s modes are activated, generating the most energetic waves of the IG band inside the harbor. Accordingly, the latter will be able to amplify the horizontal motions of ships when their oscillation periods coincide, generating port-ship resonance.

3.2. Moored ship motions

Wave energy variations are transferred to ship motions, generally in a direct relationship. Moreover, when the oscillation period of the ship coincides with that of the waves, the motions are amplified by resonance. Horizontal motions (yaw, sway and surge), whose oscillation periods are in the IG band (López and Iglesias, 2014), may coincide with infragravity waves. Due to the operational risk of these motions, in this section, the behavior of moored ships is studied and discussed, based on the results from the hydrodynamics described above: eigenmodes and location of nodes and antinodes.

The behavior of three vessels, bulk carriers between 179 and 225 m in length, representative of the fleet that docks at the studied berth was analyzed in this work. These ships were Nord Saturn (225 m), Nautical Lucia (200 m) and Aloe (179 m), whose operations were conducted in zones Z4 and Z5 of berth A1. Tables 1 and 2 outline the main characteristics of these ships and their operation, as well as the sea-state and marine weather data during their monitoring.

3.2.1. Nord Saturn

The ship Nord Saturn (225 m long) was monitored for 60 h while unloading bauxite in zone Z5. During the first 21 h, the short wave significant wave height, Hs, recorded by the tide gauge, reached values of approximately 0.3 m. Subsequently, a storm event increased this parameter to 0.6 m during the remaining monitoring time. In this last period, the storm peaked between 6 and 11 am on the second day, reaching 0.9 m significant wave height. This change in wave condition made it possible to divide Fig. 6 and Fig. 7 in two sections to facilitate understanding: a calm and a storm time interval.

Wave data (Fig. 6) showed these two phases in both frequency-filtered logs and WTA. The latter represents the energy in colors corresponding to each period (Y axis) and instant of time (X axis), with the maximum energy in red and the minimum in blue. The energy of the IG (30–150 s) and FIG (150–300 s) bands was proportional to that of the short wave, reaching the maximum at the peak of the storm. This result was identified by analyzing the amplitudes in Fig. 6a and the energy packets represented in colors in Fig. 6b. In FFT, the most energetic period was 132 s, followed by 102 s. In the WTA, the energy packets corresponding to these periods seemed to merge into a single one, indicated with a red horizontal line the period of 132 s. Additionally, in the IG band of the spectrum, different peaks of shorter period with significantly lower energy were identified, as discussed in Section 3.1.

The results from the WTA of the ship motion records (Fig 7) presented similar patterns in terms of oscillation periods and their variation over time. In general, the period of these motions, which are related to under keel clearance (UKC), were proportional to the tide, with an upward trend due to the unloading process and the resulting change in weight and draft of the vessel. Other explanation could be a mooring issue: the crew usually tighten lines at high tide and if they are not taking care of them, at low tide mooring lines are slacker. In any way, the sway and yaw period in this type of vessel is directly related to the factor δ (water depth/vessel draft), similarly to the surge of the LPGs studied in Costas et al. (2022). The sway and yaw amplitudes were proportional and higher in the second section when the energy of the waves was greater (color in Fig. 7a and b). However, the maximum values did not

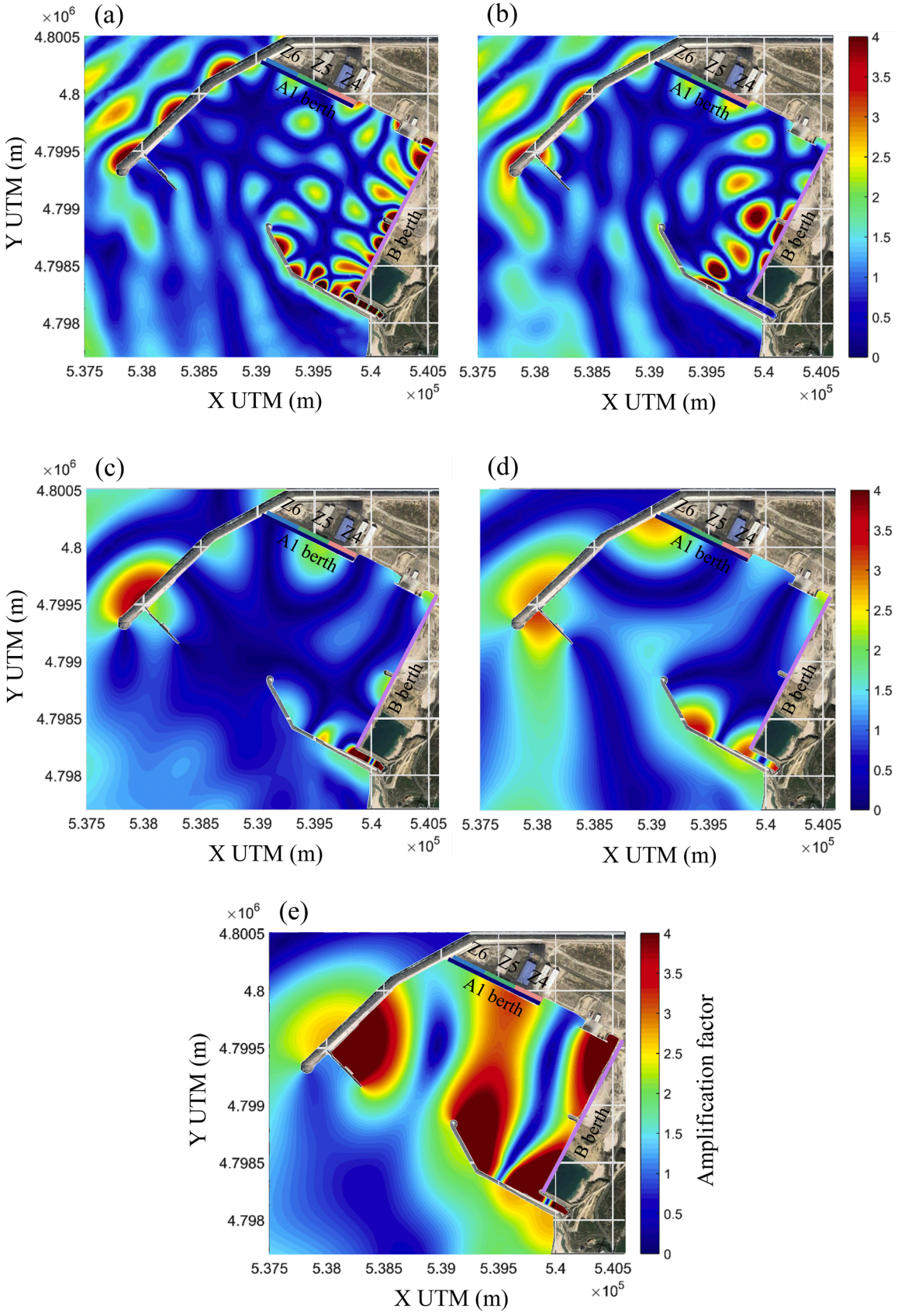

Fig. 5. Eigenmodes maps for the mean water level and NW direction of the selected resonant modes: (a) 34 s, (b) 40 s, (c) 76 s, (d) 102 s and (e) 132 s.

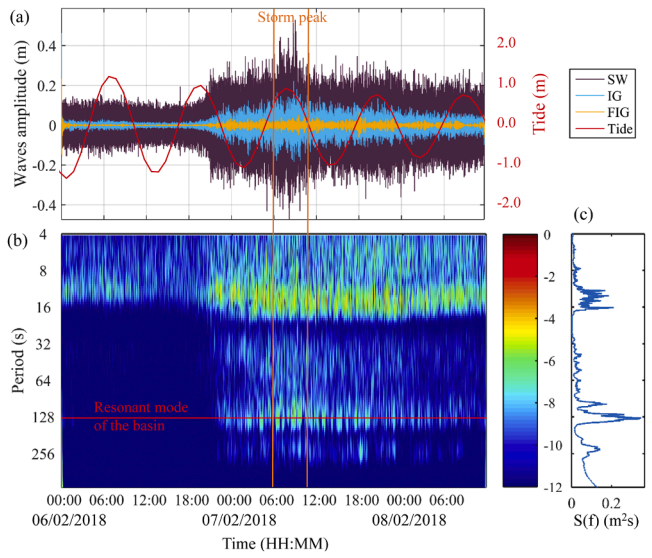

Fig. 6. (a) Records filtered by frequency, (b) WTA and (c) FFT of the Miros radar during the monitoring of the ship Nord Saturn.

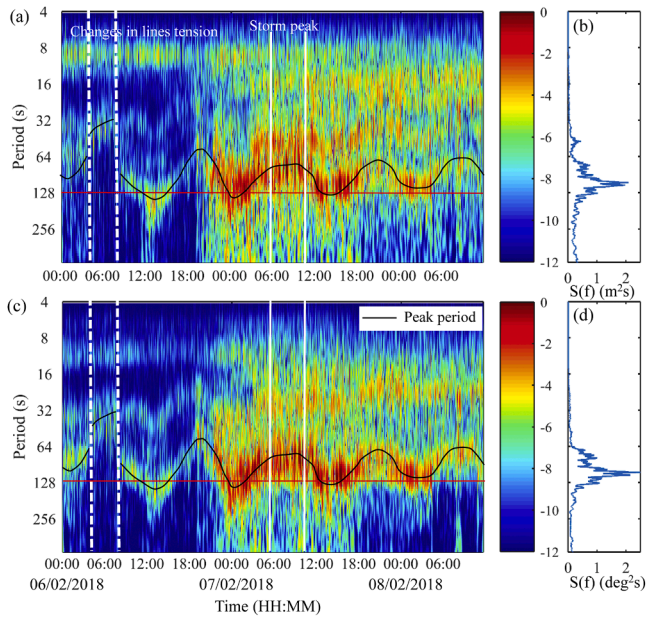

Fig. 7. (a) WTA and (b) FFT of the sway motion in the midpoint (c) WTA and (d) FFT of the yaw motion of the ship Nord Saturn.

coincide with the peak of the storm, but with resonant events between the harbor and the ship. The variation of the periods resulted in their coincidence with the resonant modes of 102 and 132 s in all low tides (higher amplitudes represented by red packets in Fig. 7a and c). The exception was the first low tide, presumably caused by the higher tension of the moorings and change in cargo onboard. In addition, jumps in the period were detected and marked by vertical dashed lines, most likely due to a change in the configuration or tension of moorings.

During the monitoring interval, the bow of the ship was sometimes far from the berth (Fig. 8b), coinciding with the low tides, except for the first (the only low tide without resonance). With more freedom of motion, the oscillation periods should increase, as observed in sway and yaw (Fig. 7a and c). Because of this increase, the motions entered into resonance with the 102 and 132 s modes, amplifying the amplitudes. Mooring configuration and tension play a key role in resonance. In this case, the configuration was asymmetrical with 6 lines on the stern and 4 on the bow (Table 2 and Fig 8d). Although the pretention is unknown, the usual practice in the operation of the study ships is the manual tensioning of the mooring lines because the ships lack constant tension winches. For this reason, pretension is adapted to high tide (maximum elevation of the ship-maximum tension in the moorings). This procedure causes a gradual slackening of the mooring lines during the descending tide cycle, which results in a less restricted motion.

After analyzing the variations of possible meteorological forcing over time, in addition to tide, the wind effect on this behavior was considered a relevant aspect in this study. The location of the Outer Port of Punta Langosteira registers significant and especially intense maximum winds, which can affect the dynamic behavior of moored ships. During much of the recording period, the wind was blowing in a direction of 30°–90° from land to sea, separating the ship from the berth (Fig. 8b), at speeds of up to 60 km/h (Fig. 8c). At 8:00 pm, on the second day, the wind shifted to a direction of 140°, blowing from sea to land. Although the wind action tended to squeeze the ship against the marine fenders, the ship kept her bow away from the berth. This change was accompanied by a decrease in wind intensity, to speeds below 20 km/h, which limited the wind effect on the position of the ship in the berth. Thus, in view of this relationship, wind was analyzed for the three study vessels to identify its influence on the moored vessel motion behavior in detail.

3.2.2. *Nautical Lucia*

The 200 m-long ship Nautical Lucia was monitored for 50 h during the clinker loading operation in zone Z5. The sea states of this interval remained constant with a NW direction and a mean significant wave height of 1.56 m at the buoy, and 0.3 m at the Miros radar buoy (Table 2). The temporal records of this radar were filtered by frequency bands to calculate their associated amplitudes. Also the WTA and FFT were represented. Fig. 9a shows that the wave amplitudes of each frequency range (SW, IG and FIG) experience some modulation with the tidal cycles because the waves are more energetic during high tides than during low tides. Additionally, in relation to the short wave energy, the infragravity energy is almost zero (Fig. 9c), in contrast to the mooring of the ship Nord Saturn (Fig. 6c). This is consistent with general knowledge of IG waves; lower energy levels of shorter period lead to lower IG energy levels.

The results from the WTA of the time series of the sway and yaw motions of the ship Nautical Lucia show the same pattern of period variation throughout the frequency range (Fig. 10a and c). In short wave band, both motions oscillated with the same period as the swell and with proportional energy. In the IG band, the sway oscillates with a period around 40 s and the yaw around 35 s. Additionally, two behaviors that occurred simultaneously in both motions were differentiated: in two sections of the record (the first and third), a single peak period was expressed, and in two other sections (second and fourth), two oscillation periods were detected around 30 and 100 s. These sections were divided with vertical lines and numbered (I, II, III, IV) in Fig. 10a and c for clarity. When the motions oscillated with a single period, the amplitudes were larger in the sway motion than when periods coexisted. This pattern was reversed in the yaw motion, reaching higher amplitudes during the intervals of coexistence of the two oscillation periods.

The situations in which two periods were detected, coincide with two high tides in which the bow was far from the berth (Fig. 11b). The wind analysis showed that the direction remained constant around 140°, that is, pushing the ship against the berth. Nevertheless, the speed was lower than 5 km/h when the bow moved away from the berth (Fig. 11c). In other words, as the wind disappeared as a forcing, the bow separated from the fenders, most likely due to insufficient mooring tension. This changed the vessel mooring system and consequently the motion behavior of the vessel, leading to different motion amplitudes. Accordingly, the action of the wind has an indirect effect on the behavior of ship motions by contributing to changes in their oscillatory frequency, which can affect port-ship resonance.

As expected, the temporal variation of the periods is affected by tidal

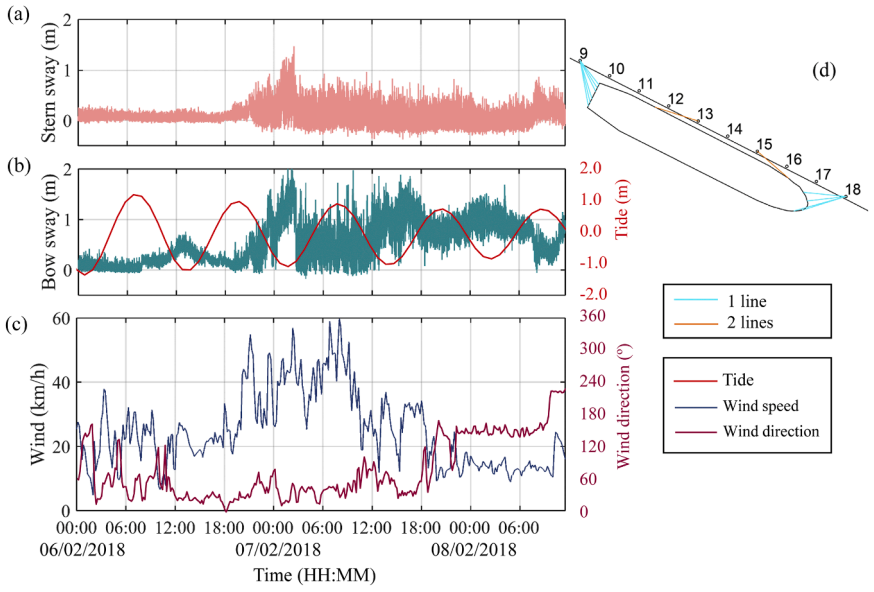

Fig. 8. (a) Record of stern and (b) bow sway, (c) wind speed and direction and (d) mooring configuration during the monitoring period of the ship Nord Saturn.

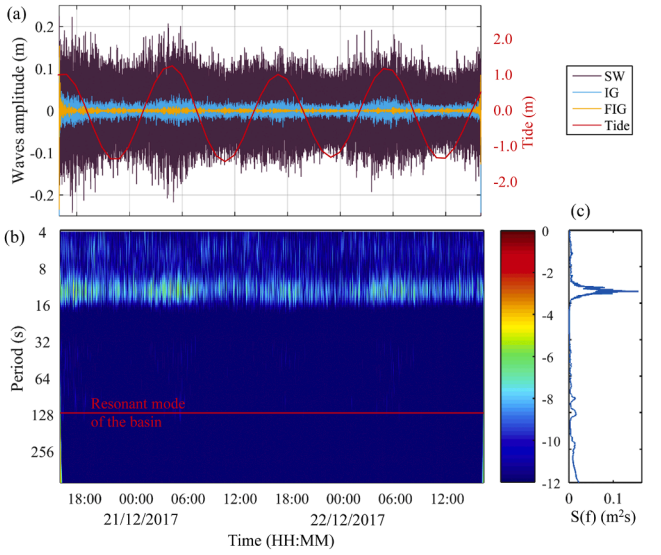

Fig. 9. (a) Records filtered by frequency, (b) WTA and (c) FFT of the Miros radar during the monitoring of the ship Nautical Lucia.

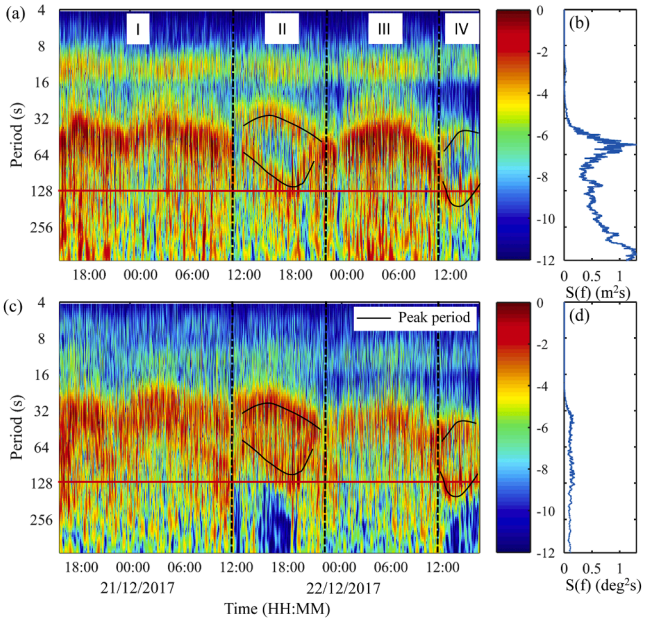

Fig. 10. (a) WTA and (b) FFT of the sway motion in the midpoint (c) WTA and (d) FFT of the yaw motion of the ship Nautical Lucia.

effects and loading status (Fig. 10a and c). However, the ranges of variation were more limited than those of the previously analyzed ship (Nord Saturn), possibly due to the mooring configuration and/or tension because the smaller the tension is, the wider the oscillation periods and ranges of variation will be. The recorded data suggest that the Nord Saturn ship had more relaxed mooring lines since the maximum distance in the position of the bow away from the fenders reached 1 m (Fig. 8b), in contrast to 0.4 m in Nautical Lucia (Fig. 11b).

3.2.3. Aloe

The 179-m-long ship Aloe was monitored for 51 h while unloading wheat in zone Z4. During this period, the incident swell remained relatively constant. The mean significant wave height was 2.89 m at the buoy and 0.27 m at the tide gauge (Table 2). The record decomposed by period ranges (swell, IG and FIG), as well as the energy in the frequency-and-time domain (WTA) is represented in Fig. 12 showing no significant changes in swell and the expected modulation with the tide, reaching higher amplitudes in high tide, a recurring pattern at all frequencies. The expected peaks at 102 and 132 s were the most energetic in the IG band. Moreover, lower energy peaks can be seen at higher frequencies in this band. In the FIG band it is worth noting the 250 s period despite the fact that no influence on vessel motion was observed.

Given the fairly constant weather and wave conditions, the behavior of the ship should have remained constant over time. However, in the first half of the record, the amplitudes were lower than in the second. The different behavior in the first and second half of the time series may be caused by the slight change in swell period from 12 to 14/15 s. The graphs constructed by applying WTA to the sway and yaw motions are shown in Fig. 13a and c. These figures also show the proportionality between the oscillation period and the factor δ, which implies the variation caused by the tide, as well as the increasing trend caused by the unloading effect on the vessel draft during its mooring at the port.

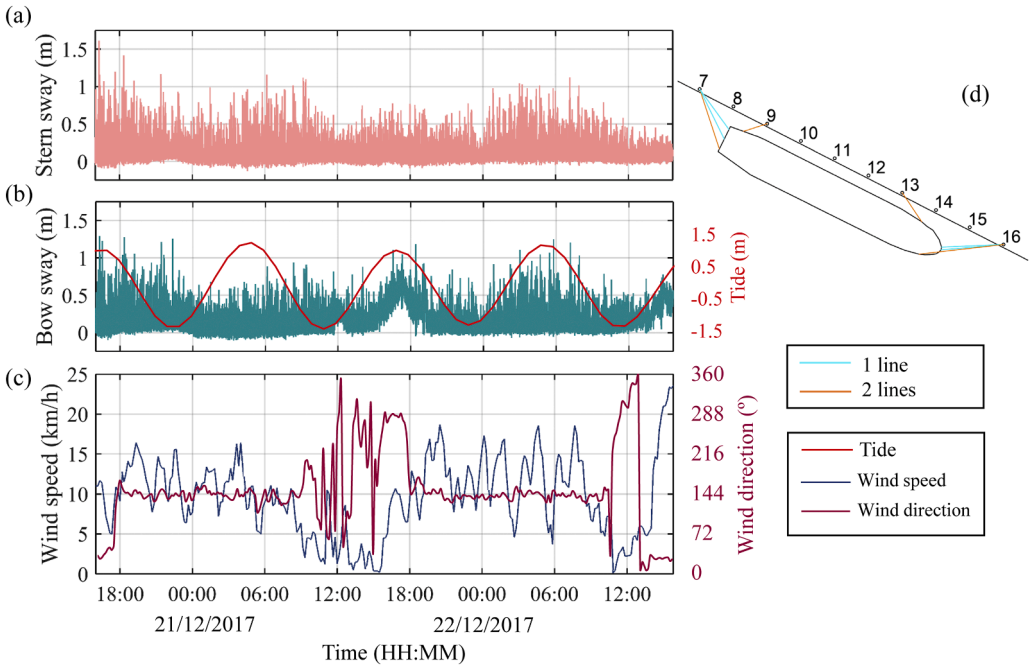

Fig. 11. (a) Record of stern and (b) bow sway, (c) wind speed and direction and (d) mooring configuration during the monitoring period of the ship Nautical Lucia.

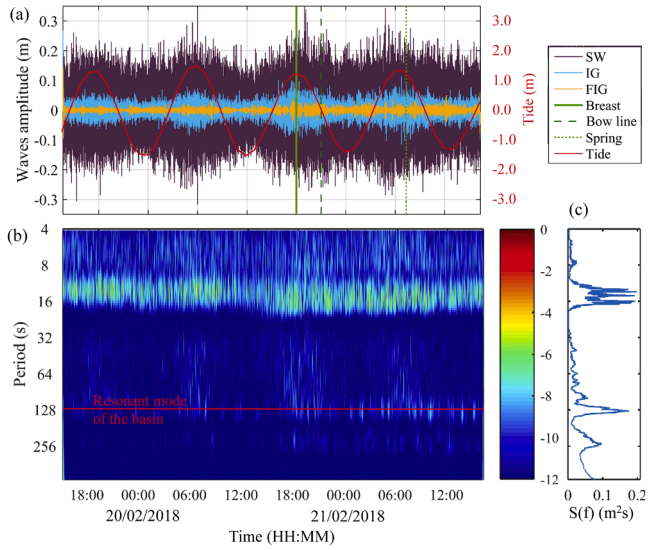

Fig. 12. (a) Records filtered by frequency, (b) WTA and (c) FFT of the Miros radar during the monitoring of the ship Aloe.

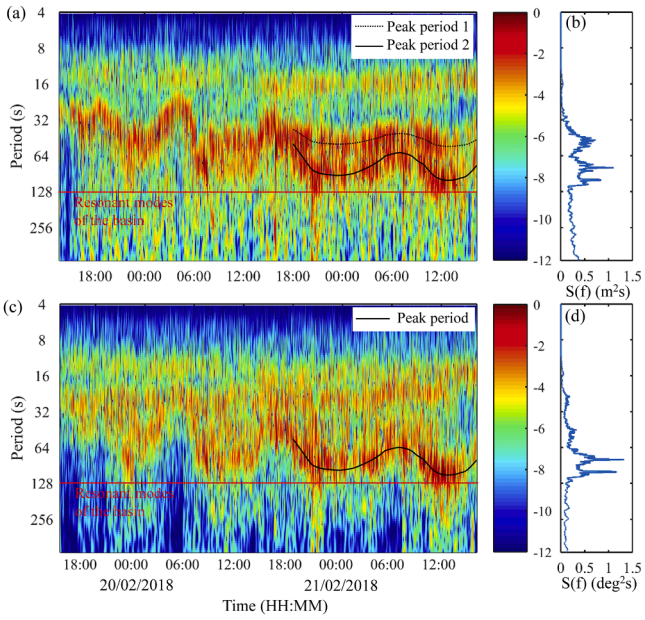

Fig. 13. (a) WTA and (b) FFT of the sway motion in the midpoint (c) WTA and (d) FFT of the yaw motion of the ship Aloe.

In the second half of the record, two oscillation periods were identified in the sway motion (black lines in Fig. 13a), entering one of them in resonance with the 102 s mode. The resonance was more notable at low tides since the period was slightly lower and moved away from the critical resonant period at high tides, generating smaller amplifications. The energy packets corresponding to the longest period of sway (continuous black line in Fig. 13a) were detected in the same way in the yaw motion, as the only oscillation period in the IG band (black line in Fig. 13c). The comparison of both graphs suggests that the resonant yaw motion could induce an oscillation in the sway motion. This would explain the appearance of two periods: one of the sway itself and the other induced by the yaw. The latter occurred when the yaw had sufficient energy, as in this case, in a resonance event.

Although yaw reached the resonant period of the harbor only in two low tides of the four tidal cycles, this resonant period appeared as the first peak period in FFT (Fig. 13d). By contrast, sway showed the same energy in both periods, despite the period induced by yaw appearing only from the middle of the record (Fig. 13b), which highlights its importance.

During the period when resonance is identified, in the second half of the record, the bow was far from the berth, particularly at low tides (Fig. 14b). That was due to an insufficient tension of the moorings and to the wind action, which blowed from land (24°–50°), separating the ship from the berth, with an increasing of wind intensity over time during monitoring. When the bow separated (final half of the record), the wind speeds were higher than 20 km/h (Fig. 14c), causing the ship to move away from the fenders and increasing the oscillation periods of the

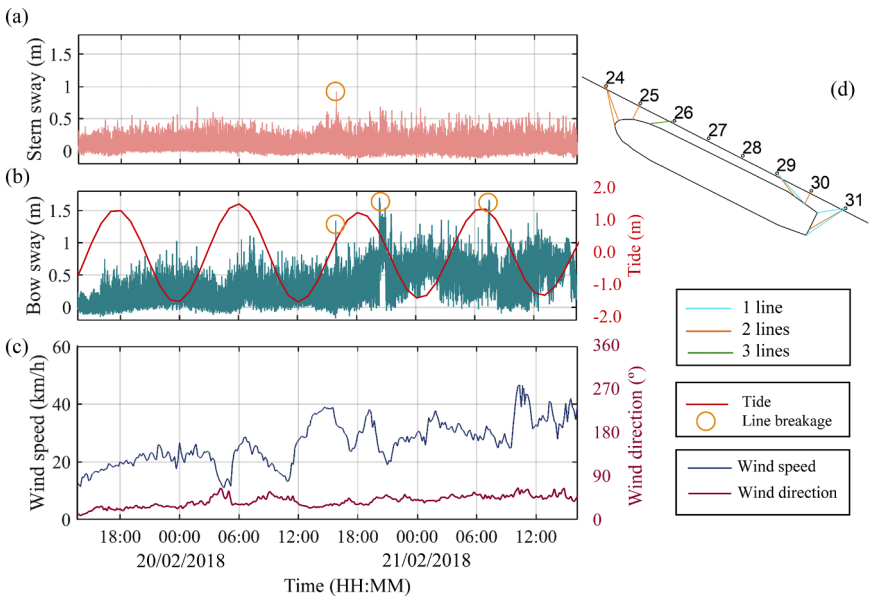

Fig. 14. (a) Record of stern and (b) bow sway, (c) wind speed and direction and (d) mooring configuration during the monitoring period of the ship Aloe.

vessel that generated resonance between the harbor and the ship.

The ship Aloe experienced three breaks of the bow mooring lines while docked at the port, which do not coincide with peaks or variations of the main forcing, the swell (Fig. 12). However, they occurred concurrently with the three maximum values of bow sway (Fig. 14b). Moreover, the maximum and significant statistics of the yaw record were obtained every 20 min (Fig. 15). The extreme values in the maximum twenty minutes of the yaw motion coincide with the three breaks. Similar values were recorded in motions that did not produce breakage, which suggests that maximum motion may be a sufficient but not necessary condition and that other factors may also be involved, such as the asymmetric distribution of tensions among the mooring lines.

3.3. Downtimes analysis

Vessel movements are the response to the different meteorological forcing to which they are exposed. These motions can cause downtimes, compromising the safety of operations and leading to economic losses. For this reason, the climatic parameters that define the data waves inside and outside the basin, tidal and wind of the sea states prior to and during 12 intervals of port downtime in the Outer Port of Punta Langosteira were studied in this section. Information concerning the date and time of 7 downtimes related to operability and 5 downtimes related to safety between 2017 and 2022 was available. In the first ones, the master of the vessel ordered the interruption of loading or unloading and in the second ones, the master also requested to leave the berth. Thus, they were analyzed separately in the following sections.

3.3.1. Operability

Downtime information was available for seven vessels with lengths between 90 and 180 m, six of which carried solid bulk (stop loading/unloading) and one general cargo (low performance). All of them were operating at berth A1. The data taken into account for the analysis of this problem were the sea states corresponding to the stay of the vessels at the berth. The hours between 7am and 8pm were selected because are the usual hours of operation.

The relationship between the different wave parameters at the buoy and at the tide gauge, wind and tide of the sea states that caused downtime, as well as those prior to the problems is shown in Fig. 16. The hours when each vessel did not operate are marked in color, and all hours when any of the vessels were at the berth operating are marked in blue. In addition to this and the axis variables, the IG wave height of the 70–150 s range is presented by marker size. This band was represented as it is the most energetic and most relevant in case of resonance, as discussed in Section 3.1.

A clear influence of the significant wave height and the period as recorded at the buoy on the downtimes was detected (Fig. 16a). In fact, it was possible to define a threshold relating these two variables with the following shape: $T_p = -2.35 \cdot H_s + 29.18$ (green line in Fig. 16a). All the sea states in which the vessels presented problems to operate were above this line, with the exception of the vessel Ameland. It should be noted

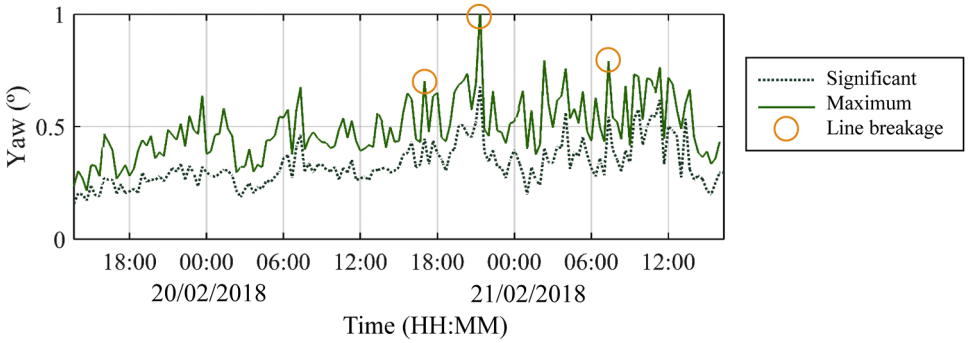

Fig. 15. Significant and maximum twenty-minute values of the yaw motion of the ship Aloe, highlighting with a circle the instants when the 3 mooring lines broke.

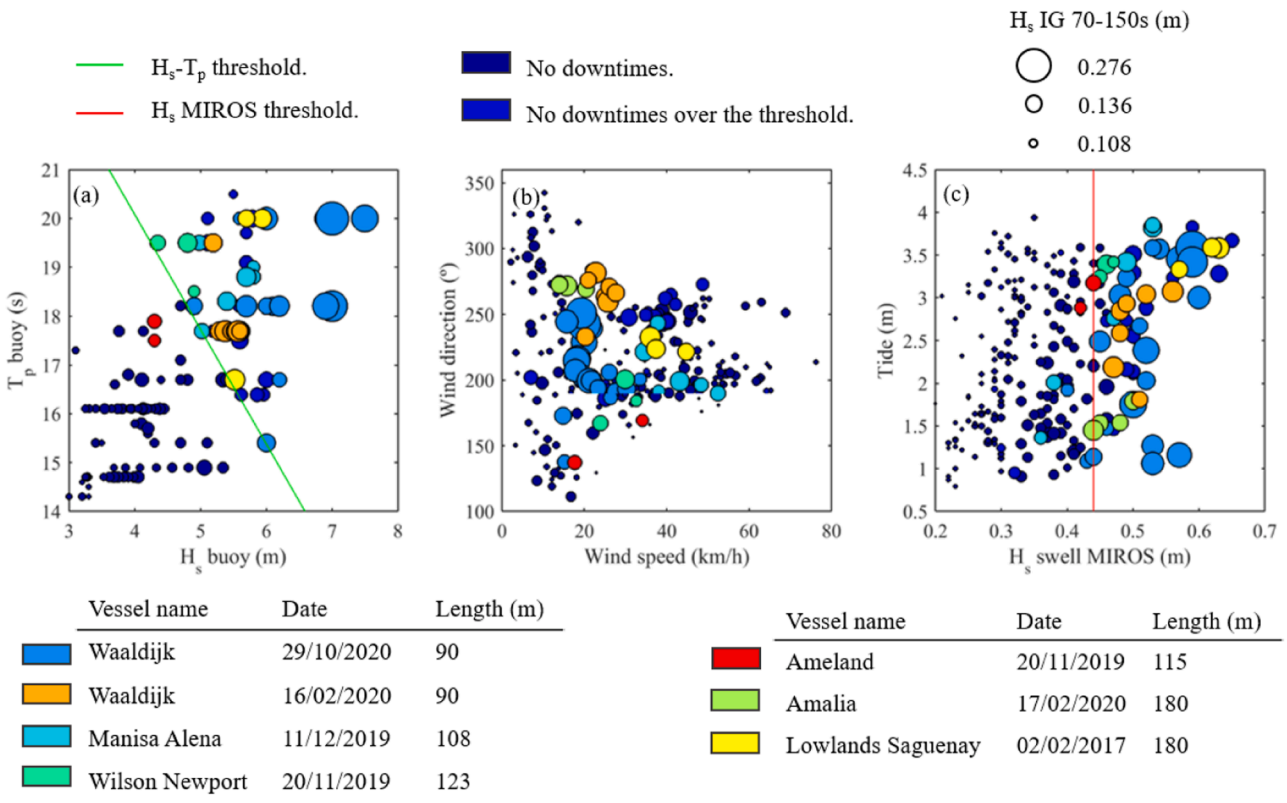

Vessel name	Date	Length (m)
Waaldijk	29/10/2020	90
Waaldijk	16/02/2020	90
Manisa Alena	11/12/2019	108
Wilson Newport	20/11/2019	123

Vessel name	Date	Length (m)
Ameland	20/11/2019	115
Amalia	17/02/2020	180
Lowlands Saguenay	02/02/2017	180

Fig. 16. Bubbleplots of significant IG 70-150 wave with (a) Hs and Tp buoy, (b) wind speed and direction and (c) Hs at tide gauge and tide, highlighting in colors the operability downtimes of each vessel.

that this vessel suffered a low performance, but it did not stop cargo operations as the others. In addition, this is the only general cargo operation. Indeed, it was unloading pipes, which is a more delicate operation than loading or unloading solid bulk with grab.

In all situations, the wind blew from sea to land (200–260° referenced 0° in the north), which implies an incidence on the vessel's side

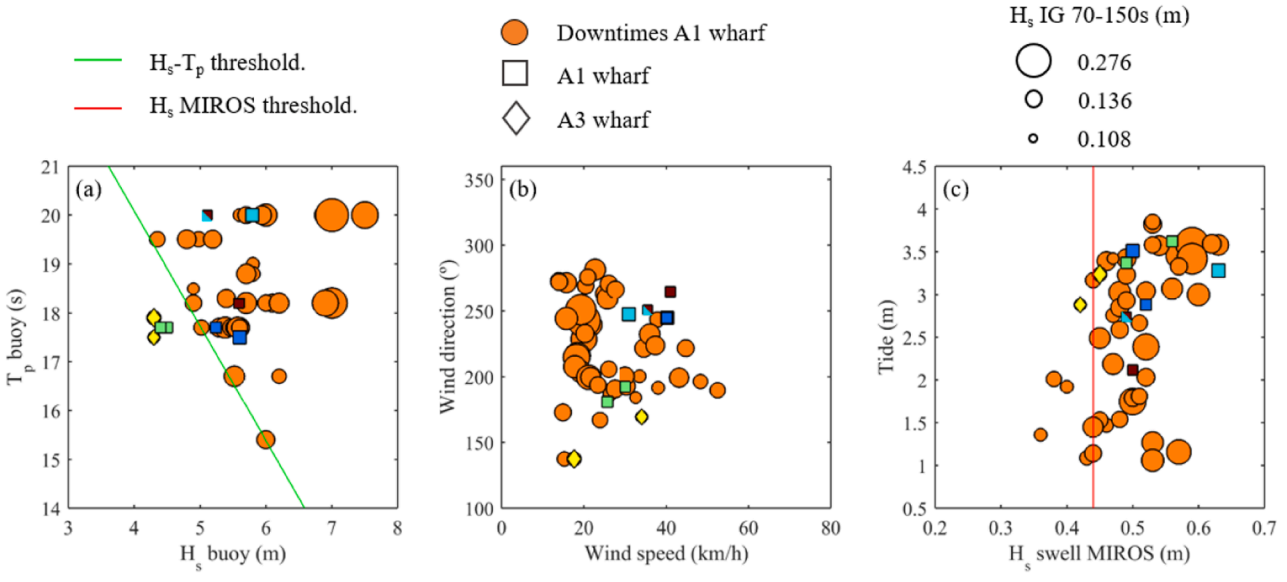

Vessel name	Date	Length (m)
John Paul K	02/02/2017	90
Fulda	02/02/2017	100
Zealand Beatrix	12/11/2019	134

Vessel name	Date	Length (m)
Juergen K	13/02/2020	89
Rose	20/11/2019	101

Fig. 17. Bubbleplots of significant IG 70-150 wave with (a) Hs and Tp buoy, (b) wind speed and direction and (c) Hs at tide gauge and tide, highlighting in colors the safety downtimes of each vessel and operability downtimes.

between 100° and 30° measured from the bow of the vessel towards the sea, respectively, with speeds above 15 km/h (Fig. 16b). With regard to the tide, operational stops are observed at all levels (Fig. 16c). Thus, wind and tide do not seem to be determining factors according to the available data. Finally, the significant short wave height at the tide gauge location is generally above 0.44 m (red line in Fig. 16c), with the exception of the first two hours of the Manisa Alena vessel and the low performance of the Ameland. It should be noted that the decision to stop operation is made by the captain, thus being subjective.

Some no downtime situations (normal operation) can be identified above the threshold, not only of the H_s-T_p relationship but also of the H_s at the tide gauge. In any case, these sea states present a smaller significant wave height IG in the range 70–150 s than sea states with downtimes, which highlights the importance of taking this variable into account in the definition of an operational downtime criterion.

3.3.2. Safety

Five downtimes of different vessels with lengths between 90 and 134 m were analyzed separately. In these cases, the downtime led to the vessel leaving berth because risks were judged too high for staying in port. It should be noted again that this decision is made by the captain, so subjectivity must be taken into account. For the study of the climatic variables that produced these situations, the two sea states before the five vessels leave the berth (when the decision was made) are represented in Fig. 17. In this graph, the axes and sizes of the markers of Fig. 16 are kept. This is shown together with the sea states of operational stops analyzed in Section 3.3.1 for an easy comparison (orange circles).

The pre-departure sea states of three of the vessels are above the operational threshold of the H_s-T_p at the buoy relationship, with no difference found between the two types of downtimes (operability and safety) (Fig. 17a). However, the Juergen K and Rose vessels requested to leave the berth when the threshold was not exceeded. The Rose vessel was the only one at berth A3, including the vessels with operational downtimes. Therefore, the limit is not appropriated for this area of the basin. In any case, the significant wave height on the tide gauge the hour before departure exceeded 0.44 m (Fig. 17c). It should be noted that these two hours are the same sea states as the low performance time of the Ameland vessel (berth A1). Likewise, the H_s threshold at the MIROS in the case of the Juergen K was also exceeded (Fig. 17c).

The data of the three vessels located above the threshold of Fig 17a, correspond to winds above 30 km/h blowing in a 250° direction (forming 45° with the longitudinal of the vessel from the sea side). Concerning the tide, the five vessels requested anchorage at levels above mean tide (2 m). However, the data are not sufficient to draw a conclusion about the influence of these variables.

To sum up, the weather conditions that led to the decision to stop the (un)loading and leave the berth are in the range of sea states that only led to operational shutdown. This may be due to the subjectivity of the decision and/or to the appearance of another problem not detectable with the study of meteorological forcing such as port-ship resonance. For this reason, it is necessary to continue the research as more information is obtained regarding downtimes in this and other ports in the world.

4. Conclusion

The present study analyzes the effect of harbor eigenmodes and wind on the infragravity motions of sway and yaw of moored ships of the Outer Port of Punta Langosteira (A Coruña, Spain). For this purpose, harbor resonant modes maps and amplification factor curves were obtained from a numerical model, whose the frequencies of the eigenmodes were validated with field measurements. Based on nodes and antinodes distribution, the ship motions were analyzed in the time-frequency domain by Wavelet Transform Analysis next to the study of climatic data. Aditionally, the forcings of 12 intervals of port downtime were studied leading to the propose of two operability thresholds that help to optimize ship stays, to avoid downtimes, and to advance the safety of loading and unloading operations.

Only the 102 and 132 s resonant modes are excited, most likely because the energy coming from outside is in this frequency range. Therefore, in the studied harbor, port-ship resonance events occur when the periods of the ship motions are close to or higher than 100 s.

The infragravity periods of the sway and yaw motions, in bulk carriers between 179 and 225 m, are proportional to the factor δ (water depth/vessel draft). Additionally, the wind can modify the position of the ship with respect to the berth when the lines were slack (tightening or separating) and when it separates the periods of the motions increases. In some cases, when the ship moved away from the fenders, the oscillatory period of the motion coupled with one of the natural periods of the harbor (102 s), causing port-ship resonance, thereby amplifying the motions. The wind effect was decisive, particularly when its intensity exceeded 20 km/h, blowing with a component perpendicular to the centerline of the ship and thus highlighting the importance of including its analysis in studies on moored ship behavior. Mooring lines at the considered berths should be kept better under tension to avoid slack lines, especially during days with strong wind blow in land to sea direction and energetic wave conditions.

Another key finding is that sway and yaw motions are highly related to each other, as shown by their patterns in the time-frequency domain, generating motions induced by one oscillatory mode over the other. In this way, the yaw motion in resonance (high energy) induced important amplitudes in sway.

During the ship monitoring, three mooring lines broke at maximum sway and yaw values, two of which during a suspected situation of port-ship resonance. However, this condition of port-ship resonance does not fully account for such an event because no other mooring lines broke with similar amplitudes of motion at other moments during the same event and during other events. Other factors such as the asymmetric distribution of tension between mooring lines of the same type must be studied to explain such an operational risk.

Analyzing the climatic forcing of 7 downtime intervals related to operability, an operational threshold relating H_s-T_p at buoy ($T_p = -2.35 \cdot H_s + 29.18$) and a threshold for significant wave height at the gauge tide of 0.44 m were proposed. Additionally, 4 safety-related downtime events were studied. Generally, the weather conditions that triggered the decision to leave the berth are in the range of sea states that only led to operational downtime. Therefore, this incidence may be linked to the subjectivity of the decision made by the captain to leave berth and/or to the occurrence of another problem not detectable with the study of meteorological forcing such as port-ship resonance. These reasons make that a quantified general threshold for safety-related downtime could not be derived.

Last, this study shows the potential of WTA, which enables us to accurately identify port-ship resonance, improving our understanding of the phenomenon and the identification of forcing agents.

CRediT authorship contribution statement

Raquel Costas: Conceptualization, Methodology, Validation, Formal analysis, Investigation, Data curation, Writing – original draft, Visualization. **Andrés Figuero:** Conceptualization, Resources, Writing – review & editing, Project administration, Funding acquisition. **José Sande:** Conceptualization, Resources, Writing – review & editing, Project administration, Funding acquisition. **Enrique Peña:** Resources, Writing – review & editing, Supervision, Project administration, Funding acquisition. **Andrés Guerra:** Resources, Funding acquisition.

Declaration of Competing Interest

The authors declare that they have no known competing financial interests or personal relationships that could have appeared to influence the work reported in this paper.

Data availability

The authors do not have permission to share data.

Acknowledgments

This research was funded by the Spanish Ministry of Economy, Industry, and Competitiveness, R&D National Plan (BIA2017-86738-R), the Spanish Ministry of Science and Innovation, Retos Call (PID2020-112794RB-I00 / AEI / 10.13039/501100011033) and the FPI predoctoral grant from the Spanish Ministry of Science, Innovation, and Universities (PRE2018-083777). Funding for open access charge: Universidade da Coruña/CISUG. The authors are grateful to the Port Authority of A Coruña (Spain), the crew of reference vessels for their kind collaboration on board, Aquática for providing the pressure gauge data, and IHCantabria for the MSP model.

References

André, G., Bellafont, F., Leckler, F., Morichon, D., 2021. Predicting seiche hazard for coastal harbours along the northern and western coasts of France. Nat. Hazards 106, 1065–1086. https://doi.org/10.1007/s11069-021-04509-y.

Ayet, A., Chapron, B., 2022. The dynamical coupling of wind-waves and atmospheric turbulence: a review of theoretical and phenomenological models. Bound. Layer Meteorol. 183, 1–33. https://doi.org/10.1007/s10546-021-00666-6.

Bellotti, G., 2020. A modal decomposition method for the analysis of long waves amplification at coastal areas. Coast. Eng. 157, 103632 https://doi.org/10.1016/j.coastaleng.2019.103632.

Bertin, X., de Bakker, A., van Dongeren, A., Coco, G., André, G., Ardhuin, F., Bonneton, P., Bouchette, F., Castelle, B., Crawford, W.C., Davidson, M., Deen, M., Dodet, G., Guérin, T., Inch, K., Leckler, F., McCall, R., Muller, H., Olabarrieta, M., Roelvink, D., Ruessink, G., Sous, D., Stutzmann, É., Tissier, M., 2018. Infragravity waves: from driving mechanisms to impacts. Earth Sci. Rev. 177, 774–799. https://doi.org/10.1016/j.earscirev.2018.01.002.

Chen, M.Y., Mei, C.C., Chang, C.K., 2006. Low-frequency spectra in a harbour excited by short and random incident waves. J. Fluid Mech. 563, 261–281. https://doi.org/10.1017/S0022112006001273.

Costas, R., Figuero, A., Peña, E., Sande, J., Rosa-santos, P., 2022. Integrated approach to assess resonance between basin eigenmodes and moored ship motions with wavelet transform analysis and proposal of operational thresholds. Ocean Eng. 247 https://doi.org/10.1016/j.oceaneng.2022.110678.

Díaz-Hernández, G., 2006. Análisis de Resonancia Portuaria: Generación, Transitoriedad, no Linealidad y Acoplamiento Geométrico. (Port Resonance Analysis: Generation, Transient, Non-Linearity and Geometric Coupling.). Universidad de Cantabria.

Diaz-Hernandez, G., Mendez, F.J., Losada, I.J., Camus, P., Medina, R., 2015. A nearshore long-term infragravity wave analysis for open harbours. Coast. Eng. 97, 78–90. https://doi.org/10.1016/j.coastaleng.2014.12.009.

Diaz-Hernandez, G., Rodríguez Fernández, B., Romano-Moreno, E., Lara, J.L., 2021. An improved model for fast and reliable harbour wave agitation assessment. Coast. Eng. 170, 104011 https://doi.org/10.1016/j.coastaleng.2021.104011.

Feng, Z., Ying, G., Hui, M., 2020. Experimental and modelling study on the response of mooring container ships in port under medium to long period waves. Int. J. Comput. Appl. Technol. 62, 327–337. https://doi.org/10.1504/IJCAT.2020.107421.

Figuero, A., Sande, J., Peña, E., Alvarellos, A., Rabuñal, J.R., Maciñeira, E., 2019. Operational thresholds of moored ships at the oil terminal of inner port of A Coruña (Spain). Ocean Eng. 172, 599–613. https://doi.org/10.1016/j.oceaneng.2018.12.031.

Gao, J., Ji, C., Liu, Y., Ma, X., Gaidai, O., 2017. Influence of offshore topography on the amplification of infragravity oscillations within a harbor. Appl. Ocean Res. 65, 129–141. https://doi.org/10.1016/j.apor.2017.04.001.

Gao, J., Ma, X., Dong, G., Chen, H., Liu, Q., Zang, J., 2021. Investigation on the effects of Bragg reflection on harbor oscillations. Coast. Eng. 170, 103977 https://doi.org/10.1016/j.coastaleng.2021.103977.

Kumar, P.G., Rajni, 2020. Moored ship motion analysis in Paradip port under the resonance conditions using 3-D boundary element method. J. Mar. Sci. Technol. https://doi.org/10.1007/s00773-020-00701-0. M.

Gaythwaite, J.W., Mooring Analysis Task Committee, 2014. Mooring of Ships to Piers and Wharves. ASCE Book Series.

Hao, X., Shen, L., 2022. A data-driven analysis of inhomogeneous wave field based on two-dimensional Hilbert–Huang transform. Wave Motion 110, 102896. https://doi.org/10.1016/j.wavemoti.2022.102896.

Herbers, T.H.C., Elgar, S., Guza, R.T., 1995. Generation and propagation of infragravity waves. J. Geophys. Res. 100, 24863–24872. https://doi.org/10.1029/95jc02680.

Hwang, P.A., Huang, N.E., Wang, D.W., 2003. A note on analyzing nonlinear and nonstationary ocean wave data. Appl. Ocean Res. 25, 187–193. https://doi.org/10.1016/j.apor.2003.11.001.

Karathanasi, F., Karperaki, A., Gerostathis, T., Belibassakis, K., 2020. Offshore-to-nearshore transformation ofwave conditions and directional extremes with application to port resonances in the bay of sitia-crete. Atmosphere 11, 1–23. https://doi.org/10.3390/atmos11030280 (Basel).

Kwak, M.S., Jeong, W.M., Kobayasshi, N., 2020. A case study on harbor oscillations by infragravity waves. In: Proceedings of the Coastal Engineering Proceeding.

Liu, P.C., 1994. Wavelet Spectrum Analysis and Ocean Wind Waves, Wavelet Analysis and Its Applications. Academic Press, Inc. https://doi.org/10.1016/B978-0-08-052087-2.50012-8.

Liu, Y., Liang, X.S., Weisberg, R.H., 2007. Rectification of the bias in the wavelet power spectrum. J. Atmos. Oceanic Technol. https://doi.org/10.1175/2007JTECHO511.1.

López, M., Iglesias, G., 2014. Long wave effects on a vessel at berth. Appl. Ocean Res. 47, 63–72. https://doi.org/10.1016/j.apor.2014.03.008.

López, M., Iglesias, G., Kobayashi, N., 2012. Long period oscillations and tidal level in the Port of Ferrol. Appl. Ocean Res. 38, 126–134. https://doi.org/10.1016/j.apor.2012.07.006.

Lorente, P., Sotillo, M.G., Aouf, L., Amo-Baladrón, A., Barrera, E., Dalphinet, A., Toledano, C., Rainaud, R., De Alfonso, M., Piedracoba, S., Basañez, A., García-Valdecasas, J.M., Pérez-Muñuzuri, V., álvarez-Fanjul, E., 2018. ExtremeWave height events in NW Spain: a combined multi-sensor and model approach. Remote Sens. 10, 1–12. https://doi.org/10.3390/rs10010001.

Loughlin, P., Cohen, L., 2010. Wavelets: A comparison with the spectrogram and other methods for time-frequency analysis. J. Acoust. Soc. Am. 127, 1936. https://doi.org/10.1121/1.3384871.

Massel, S.R., 2001. Wavelet analysis for processing of ocean surface wave records. Ocean Eng. 28, 957–987. https://doi.org/10.1016/S0029-8018(00)00044-5.

Mei, C.C., Agnon, Y., 1989. Long-period oscillations in a harbour induced by incident short waves. J. Fluid Mech. 208, 595–608. https://doi.org/10.1017/S0022112089002958.

European Marine Observation and Data Network. EMODnet. European Commission. 2022 [WWW Document]. URL https://www.emodnet-bathymetry.eu/ (accessed 5.10.21).

Nielsen, U.D., 2017. A concise account of techniques available for shipboard sea state estimation. Ocean Eng. 129, 352–362. https://doi.org/10.1016/j.oceaneng.2016.11.035.

Niu, X., 2020. Conditions for the occurrence of notable edge waves due to atmospheric disturbances. Appl. Ocean Res. 101, 102255 https://doi.org/10.1016/j.apor.2020.102255.

Nogueira, H.I.S., van der Ven, P., O'Mahoney, T., De Loor, A., van der Hout, A., Kortlever, W., 2018. Effect of density differences on the forces acting on a moored vessel while operating navigation locks. J. Hydraul. Eng. 144, 04018021 https://doi.org/10.1061/(asce)hy.1943-7900.0001445.

Peña, E., Figuero, A., Sande, J., Guerra, A., Perez, J.D., Maciñeira, E., 2017. Integrated System to Evaluate Moored Ship Behavior, 7A. Ocean Engineering. ASME. https://doi.org/10.1115/OMAE2017-61110. V07AT06A003.

Pessoa, J., Fonseca, N., Soares, C.G., 2015. Numerical study of the coupled motion responses in waves of side-by-side LNG floating systems. Appl. Ocean Res. 51, 350–366. https://doi.org/10.1016/j.apor.2015.01.012.

Puertos del Estado, Autoridad Portuaria de A Coruña, 2021 [WWW Document]. A Coruña Port Auth. URL http://cma.puertocoruna.com/ (accessed 10.23.20).

Puertos del Estado (Spanish Port Autority) [WWW Document URL http://www.puertos.es/es-es/oceanografia/Paginas/portus.aspx (accessed 10.23.20) 2022.

Rabinovich, A.B., 2009. Seiches and harbor oscillations. Handbook of Coastal and Ocean Engineering. In: Young C. Kim (Ed.), In: Handbook Coastal Ocean Engineering Expandad Edition, 1-2. World Scientific Publ., pp. 243–286. https://doi.org/10.1142/9789813204027_0011

Rupali, Kumar, P., Rajni, 2021. Moored ship motion under the resonance conditions with breakwaters: a coupled numerical approach. Ocean Eng. 241, 110022 https://doi.org/10.1016/j.oceaneng.2021.110022.

Sakakibara, S., Kubo, M., 2008. Effect of mooring system on moored ship motions and harbour tranquillity. Int. J. Ocean Syst. Manag. 1, 84–99.

Sammartino, S., Garrido, J.C.S., Delgado, J., Naranjo, C., Aldeanueva, F.C., Lafuente, J. G., 2014. Experimental and numerical characterization of harbor oscillations in the port of Málaga. Spain. Ocean Eng. 88, 110–119. https://doi.org/10.1016/j.oceaneng.2014.06.011.

Sande, J., Figuero, A., Tarrío-Saavedra, J., Peña, E., Alvarellos, A., Rabuñal, J.R., 2019. Application of an analytic methodology to estimate the movements of moored vessels based on forecast data. Water 11. https://doi.org/10.3390/w11091841 (Switzerland).

Kumar, V.S., Mandal, S., 2022. Characteristics of individual surface waves measured by moored buoys in the coastal waters of the eastern Arabian Sea. Ocean Eng. 248, 110861 https://doi.org/10.1016/j.oceaneng.2022.110861.

Seetharam, K., Lerose, A., Fazio, R., Marino, J., 2022. Dynamical scaling of correlations generated by short- and long-range dissipation. Phys. Rev. B 105, 1–16. https://doi.org/10.1103/physrevb.105.184305.

Stuart, D., Toms, G., Luger, S., Rossouw, M., 2014. Characterising long wave agitation in the port of Ngqura using a Boussinesq wave model. In: Proceedings of the Coasal. Engineering Conference January. https://doi.org/10.9753/icce.v34.currents.30.

Thiebaut, S., McComb, P., Vennell, R., 2013. Prediction of coastal far infragravity waves from sea-swell spectra. J. Waterw. Port Coast. Ocean Eng. 139, 34–44. https://doi.org/10.1061/(asce)ww.1943-5460.0000166.

Thotagamuwage, D.T., Pattiaratchi, C.B., 2014. Observations of infragravity period oscillations in a small marina. Ocean Eng. 88, 435–445. https://doi.org/10.1016/j.oceaneng.2014.07.003.

Torrence, C., Compo, G.P., 1998. A partical guide to wavelet analysis. Bull. Am. Meteorol. Soc. 79, 61–78. https://doi.org/10.1175/1520-0477(1998)079<0061:Apgtwa>2.0.Co;2.

Troch, C., Terblanche, L., Henning, H., 2020a. Modelling and measurement of low-frequency surge motion associated with extreme storm conditions in the Port of Cape Town. Appl. Ocean Res. 102452 https://doi.org/10.1016/j.apor.2020.102452.

Troch, C., Terblanche, L., Rossouw, M., Ntantala, Z., du Plessis, G., 2020b. Long-wave mitigation study for the Port of Ngqura. In: Proceedings of the Coastal Engineering Proceeding, p. 14.

van der Molen, W., Monárdez, P., van Dongeren, A., 2006. Numerical Simulation of Long-Period Waves and Ship Motions in Tomakomai Port. Japan. Coast. Eng. J. 48, 59–79. https://doi.org/10.1142/s0578563406001301.

van der Molen, W., Santander, P.M., van Dongeren, A., 2004. Modeling of Infragravity Waves and Moored Ship Motions in Tomakomai Port. Harbor Long Wave, Yokosuka, Japan, pp. 1–8.

van der Molen, W., Scott, D., Taylor, D., Elliott, T., 2015. Improvement of mooring configurations in Geraldton harbour. J. Mar. Sci. Eng. 4, 1–20. https://doi.org/10.3390/jmse4010003.

van Deyzen, A.F.J., Beimers, P.B., van Der Lem, J.C., Messiter, D., De Bont, J.A.M., 2015. To improve the efficiency of ports exposed to swell. In: Proceedings of the Australasian Coasts Ports Conference, pp. 919–926.

van Dongeren, A., de Jong, M., van der Lem, C., van Deyzen, A., den Bieman, J., 2016. Review of long wave dynamics over reefs and into ports with implication for port operations. J. Mar. Sci. Eng. 4 https://doi.org/10.3390/jmse4010012.

Wang, G., Dong, G., Perlin, M., Ma, X., Ma, Y., 2011. An analytic investigation of oscillations within a harbor of constant slope. Ocean Eng. 38, 479–486. https://doi.org/10.1016/j.oceaneng.2010.11.021.

Weiler, O.M., Dekker, J., 2001. Mooring cointarner ships exposed to long waves. WL/Delft Hydraulics, P.O. Box 177, 2600. http://resolver.tudelft.nl/uuid:c551b9b6-c092-43c7-acd1-018b804880c9.

Wilson, B.W., 1954. Generation of long-period seiches in Table Bay, Cape Town, by barometric oscillations. Eos Trans. Am. Geophys. Union. https://doi.org/10.1029/TR035i005p00733.

You, J., Faltinsen, O.M., 2015. A numerical investigation of second-order difference-frequency forces and motions of a moored ship in shallow water. J. Ocean Eng. Mar. Energy 1, 157–179. https://doi.org/10.1007/s40722-015-0014-6.

Yu, Y., Shenoi, R.A., Zhu, H., Xia, L., 2006. Using wavelet transforms to analyze nonlinear ship rolling and heave-roll coupling. Ocean Eng. 33, 912–926. https://doi.org/10.1016/j.oceaneng.2005.05.014.

Miros radar, 2022. Tde gauge model. [WWW Document]. URL https://www.miros-group.com/products/ (accessed 5.31.21).